SPECIAL
PECAN
COLLECTION

Lidar Observations of a Mesoscale Moisture Transport Event Impacting Convection and Comparison to Rapid Refresh Model Analysis

BRIAN J. CARROLL,[a,b] BELAY B. DEMOZ,[a,b] DAVID D. TURNER,[c] AND RUBEN DELGADO[b]

[a] *Department of Physics, University of Maryland Baltimore County, Baltimore, Maryland*
[b] *Joint Center for Earth Systems Technology, University of Maryland Baltimore County, Baltimore, Maryland*
[c] *Global Systems Laboratory, National Oceanic and Atmospheric Administration, Boulder, Colorado*

(Manuscript received 14 May 2020, in final form 3 November 2020)

ABSTRACT: The 2015 Plains Elevated Convection at Night (PECAN) field campaign provided a wealth of intensive observations for improving understanding of interplay between the Great Plains low-level jet (LLJ), mesoscale convective systems (MCSs), and other phenomena in the nocturnal boundary layer. This case study utilizes PECAN ground-based Doppler and water vapor lidar and airborne water vapor lidar observations for a detailed examination of water vapor transport in the Great Plains. The chosen case, 11 July 2015, featured a strong LLJ that helped sustain an MCS overnight. The lidars resolved boundary layer moisture being transported northward, leading to a large increase in water vapor in the lowest several hundred meters above the surface in northern Kansas. A branch of nocturnal convection initiated coincident with the observed maximum water vapor flux. Radiosondes confirmed an increase in convective potential within the LLJ layer. Moist static energy (MSE) growth was generated by increasing moisture in spite of a temperature decrease in the LLJ layer. This unique dataset is also used to evaluate the Rapid Refresh (RAP) analysis model performance, comparing model output against the continuous lidar profiles of water vapor and wind. While the RAP analysis captured the large-scale trends, errors in water vapor mixing ratio were found ranging from 0 to 2 g kg^{-1} at the ground-based lidar sites. Comparison with the airborne lidar throughout the PECAN domain yielded an RMSE of 1.14 g kg^{-1} in the planetary boundary layer. These errors mostly manifested as contiguous dry or wet regions spanning spatial scales on the order of ten to hundreds of kilometers.

KEYWORDS: Convection; Boundary layer; Water vapor; Lidars/Lidar observations; Model errors; Model evaluation/performance

1. Introduction

The Great Plains low-level jet (LLJ) is a primarily nocturnal phenomenon of strong southwesterly winds within the planetary boundary layer (PBL) spanning hundreds of kilometers in width and length, and is most frequent and impactful during the warm-season. LLJs provide major contributions to nocturnal convection in the region, such as mesoscale convective systems (MCSs), via convergence of the wind field and advection of moisture and temperature (Byerle and Paegle 2003; Trier et al. 2006; Pu and Dickinson 2014; Berg et al. 2015; Doubler et al. 2015; Shapiro et al. 2016). Climatological studies have shown that LLJs are responsible for nearly half of all warm-season moisture transport into the Great Plains (Higgins et al. 1997; Berg et al. 2015). The LLJ can feed moisture into convective systems or interact with its environment to produce convection initiation (CI), thus contributing to the nocturnal rainfall that can manifest as damaging storms or beneficial water supply for the agricultural region (Trier and Parsons 1993; Trier et al. 2017; Hitchcock et al. 2019; Weckwerth and Romatschke 2019).

The nocturnal surface-connected stable layer inhibits convection by common surface-based mechanisms such as solar heating and low-level convergence (e.g., Markowski and Richardson 2010). A contributing factor to the LLJ's influence on convection is that the strongest LLJ winds often sit above the surface-connected nocturnal inversion (Bonner 1968; Bonin et al. 2015), allowing production of elevated instability. In these situations the LLJ carries moist warm air above the inversion, and the high wind speeds allow transport across hundreds of kilometers with air parcels eventually reaching their level of free convection if sufficiently lifted by a synoptic front, baroclinic boundary, elevated convergence, MCS outflow, or bore waves (Trier and Parsons 1993; Augustine and Caracena 1994; Wilson and Roberts 2006; Berg et al. 2015; Trier et al. 2017; Hitchcock et al. 2019; Weckwerth and Romatschke 2019). This increase in convective potential manifests within the LLJ "core," the layer of strongest LLJ wind speed, with increases in many related diagnostic variables including convective available potential energy (CAPE), equivalent potential temperature, or wind convergence (Trier and Parsons 1993; Gebauer et al. 2018; Reif and Bluestein 2018; Lin et al. 2019).

Although nocturnal convection is common in the Great Plains, nocturnal CI (NCI) remains challenging to forecast,

Corresponding author: Brian J. Carroll, brian.carroll@umbc.edu

DOI: 10.1175/MWR-D-20-0151.1

especially in the absence of surface boundaries (Wilson and Roberts 2006; Reif and Bluestein 2018; Weckwerth et al. 2019). This is due in part to the paucity of routine thermodynamic profiling in the PBL and the limited resolution of satellite observations within the lowest few kilometers of the atmosphere (Kahn et al. 2011; Steinke et al. 2015; Weckwerth et al. 2019). Previous studies based on radiosonde and surface data or reanalysis datasets reveal the LLJ patterns already discussed but are limited in their ability to resolve some important details of the spatiotemporal evolution of the LLJ throughout its domain (e.g., Whiteman et al. 1997; Song et al. 2005; Walters et al. 2008, 2014). Targeted observations have been utilized over the years to improve our understanding of LLJs, MCSs, NCI, and their interplay. Wind, water vapor, and elastic backscatter lidars have been some of the key tools in these advanced studies, as they can continuously profile a variety of atmospheric properties from ground-based and airborne platforms. A case study of airborne differential absorption lidar (DIAL) data assimilation by Wulfmeyer et al. (2006) demonstrated major improvement to quantitative precipitation forecasting in the Great Plains. Airborne water vapor lidar has also proven useful in profiling the sharp moisture gradients of drylines and bore waves without steady-state assumptions (e.g., Koch et al. 2008; Bergmaier et al. 2014; Grasmick et al. 2018; Johnson et al. 2018; Lin et al. 2019). Tollerud et al. (2008) presented the first study examining submesoscale features of LLJ moisture transport using airborne DIAL and wind lidars. They found the lidar measurements to differ from interpolated dropsonde values by up to 25%, and argued for the importance of lidar-resolved small-scale circulations near the sharp moisture gradient at PBL or LLJ top. Schäfler et al. (2010) used airborne water vapor and wind lidars over Europe (without an LLJ) to evaluate ECMWF forecast model performance, showing a model wet bias of 17%. Passive ground-based sensors such as the atmospheric emitted radiance interferometer (AERI; Turner and Löhnert 2014) have also contributed to studies of LLJ thermodynamics and interactions with the stable boundary layer (Bonin et al. 2015; Toms et al. 2017; Johnson et al. 2018; Lin et al. 2019).

These observational studies have been complemented by modeling studies on the LLJ, and its role in convection. Modeling the evolution of LLJ wind speed has been greatly improved in recent years from an analytical and theoretical perspective (e.g., Du and Rotunno 2014; Shapiro et al. 2016) and optimized in terms of model setup using the Weather Research and Forecasting (WRF) Model (e.g., Klein et al. 2016; Smith et al. 2018). Modeling LLJ moisture transport in the mesoscale environment of NCI and MCS events has received relatively little attention, though warm-season precipitation forecasting remains challenging due in part to inaccuracies in low-level water vapor distributions (Weckwerth et al. 2004; Schumacher 2015; Geerts et al. 2017; Peters et al. 2017; Weckwerth et al. 2019). Peters et al. (2017) used radiosonde profiles to directly assess the impact of low-level moisture errors on forecasts of an MCS, finding such errors to propagate to significant errors in CAPE and convective inhibition (CIN), as well as MCS location.

The work presented here utilizes ground-based Doppler and water vapor lidars and airborne water vapor lidar observations from one night of intensive operations to explore mesoscale water vapor transport at high resolution, also incorporating radiosonde profiles to study changes to convective potential. The chosen case exemplifies many phenomena of interest for Great Plains nocturnal convection, including a strong LLJ, an MCS, NCI, and formation of an elevated most unstable layer. Applying water vapor lidar for a focused study of LLJ moisture transport is only preceded in the literature by Tollerud et al. (2008), which was relatively limited in that they only measured meridional moisture flux along two flight legs a few hours after sunrise. Recent work by Lin et al. (2019) bordered this topic, as they presented airborne Raman lidar observations near an MCS, targeting interactions between inflow (an LLJ), outflow, and the stable boundary layer. This manuscript shifts focus away from the MCS's immediate environment and instead examines moisture transport on a larger scale, incorporating measurements far upwind of the MCS, while still utilizing the full resolution of the lidar profiles to resolve submesoscale features. Comparing these fixed and mobile lidar observations to the Rapid Refresh (RAP) analysis model yields a more comprehensive exploration of model water vapor errors than exists in the literature.

2. Data and methods

a. PECAN

The observations used in this study came from the Plains Elevated Convection at Night (PECAN) field campaign. PECAN was a large multi-institutional project held from 1 June to 15 July 2015 in a domain that covered much of the Great Plains region (Geerts et al. 2017). The main goal of PECAN was to improve understanding and forecasting of nocturnal convection and related events, including the LLJ, MCSs, NCI, and bore waves.

PECAN featured six fixed ground sites (FPs) for automated and intensive operations, three research aircraft, several ground-based mobile observation platforms, and support from preexisting observation networks. This study utilizes observations primarily from two FPs and a lidar onboard the NASA DC-8 aircraft. The two FPs were named FP1 in the southern part of the PECAN domain and FP3 in the northern part of the domain, 317 km northwest of FP1. FP1 was at the Atmospheric Radiation Measurement (ARM) Southern Great Plains central facility (Sisterson et al. 2016). FP3 was in Ellis, Kansas. These FP locations and the DC-8 flight track are shown in Fig. 1. FP1 and FP3 were chosen because they are well-separated along the LLJ track and had complete data availability. No other sites had both autonomous wind and water vapor lidars.

The lidars and models used are detailed below. Other observational datasets used for this study are a Cartesian-gridded radar "mosaic" built specifically for PECAN research (UCAR/NCAR–EOL 2016b) and radiosondes launched from the FPs (Clark 2016; UCAR/NCAR–EOL 2015).

b. Lidars

Both FPs hosted commercial Doppler wind lidars (ARM Data Center 2014; Hanesiak and Turner 2016) and water vapor lidars. For measuring water vapor mixing ratio r, FP1 had the Raman lidar that has been at the site since 1996 (ARM Data Center 2015;

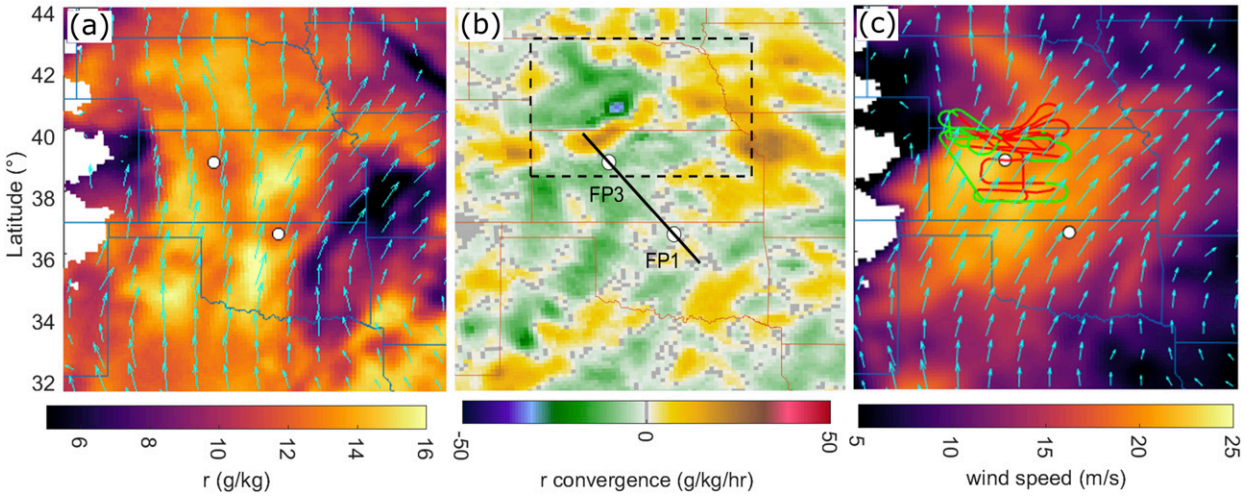

FIG. 1. RAP fields over the Great Plains for 11 Jul 2015. White circles indicate FP1 (south) and FP3 (north) locations. (a) The 850 hPa water vapor mixing ratio r at 0200 UTC with wind direction arrows. (b) Moisture convergence vertically integrated below 800 hPa at 0600 UTC, with the solid line marking the transect used in Fig. 2 and the dashed box outlining the domain of Fig. 3. (c) The 850 hPa wind speed with direction arrows at 0600 UTC, plus the DC-8 flight track in red and green. The green portion is used for LASE–RAP comparison.

Turner et al. 2016) and FP3 had a differential absorption (DIAL) system (Spuler et al. 2015; UCAR/NCAR–EOL 2016a). All four ground-based lidars were running autonomously, so this study exemplifies potential benefits of more permanent lidar profiling networks. The DC-8 carried the NASA Lidar Atmospheric Sensing Experiment (LASE) (Browell et al. 1997; Ferrare et al. 2016), a DIAL system for water vapor mixing ratio profiling. Instrument parameters for all lidars are listed in Table 1. Values reported indicate what was used in this study; e.g., FP3 DIAL minimum range is technically 225 m but was quality controlled to 450 m. Instrument quality control measures were executed at the direction of the instrument PIs. Quality control measures that are not in the referenced datasets or Table 1 are:

- FP1 water vapor lidar mixing ratio data were omitted if the reported measurement uncertainty exceeded 2.25 g kg^{-1} or 25% of the measured magnitude;
- FP3 water vapor lidar data required manual inspection and removal of data near clouds;
- FP1 Doppler lidar data were omitted if the reported measurement uncertainty exceeded 6% for wind speed or 15° for wind direction.

c. *Model: The Rapid Refresh (RAP)*

The Rapid Refresh (RAP) analysis was evaluated against measurements for its ability to produce observed moisture distribution and transport features. RAP is an hourly updated data assimilation and modeling system run operationally at the National Centers for Environmental Prediction (NCEP). RAP is run at 13 km horizontal grid spacing over North America. RAP output is archived hourly. The operational version during PECAN, and used in this study, was RAPv2. A comprehensive description of RAP is available in Benjamin et al. (2016). RAP was chosen for this study because it is often used to provide environmental context in atmospheric research (e.g., Peters et al. 2017; Stelten and Gallus 2017; Wilson et al. 2018; Degelia et al. 2019; Hitchcock et al. 2019), and it provides initial and lateral boundary conditions to the High Resolution Rapid Refresh (HRRR), a 3 km grid spacing convection-allowing modeling system.

d. *Methodology for lidar and RAP comparisons*

The lidar vertical profiles are directly compared to RAP output field profiles in this study. Only the model grid points closest to each observation location were used (e.g., the one grid box that overlapped with FP3 was used for all FP3 lidar–model comparisons). The model data were not spatially or temporally averaged, but the lidar data were to accommodate calculations using the various unique spatial and temporal resolutions involved. The following steps were taken:

- For all lidar versus RAP comparisons, the finer spatial resolution (i.e., lidar) profile was linearly interpolated to

TABLE 1. Lidar instrument and data parameters.

Lidar	Wavelength (nm)	Vertical resolution (m)	Lowest data altitude (m AGL)	Temporal resolution
FP1 Doppler	1540	26	91	15 min
FP3 Doppler	1540	50	100	15 min
FP1 Raman	355	37.5	172.5	70 s
FP3 DIAL	828.2	75	450	5 min
LASE	817	330	~350	3 min (37 km)

the coarser resolution (i.e., RAP) profile. Likewise for moisture flux calculation from wind and water vapor lidar, the finer resolution was interpolated to the coarser.
- For ground-based lidar versus RAP comparisons, the lidar observations were averaged within 15 min of the RAP hourly output times.
- Airborne lidar data were only compared to RAP within 15 min of the hourly RAP output times.
- If multiple airborne lidar profiles from the same overpass were present within a single model grid box, only the lidar profile closest to the center of the grid box was considered.
- LASE data within 50 km of radar composite reflectivity greater than 25 dBZ was removed when comparing to RAP. This was done to eliminate any highly dynamic precipitation areas from the comparison.

The red and green line in Fig. 1c shows the LASE flight track, but only the green portions (which meet the RAP output time and nearby reflectivity restrictions listed above) are used for comparison.

It is important to consider the spatial and temporal representations of these very diverse observational (and model) datasets. The averaging windows described above are meant to lessen discrepancies in representation. For example, the RAP gridbox sizes are much larger than a lidar's footprint. Temporally averaging the lidar observations as the atmosphere moves above the fixed lidar is a way of artificially increasing the lidar footprint, bringing it closer to the RAP grid resolution. The airborne lidar observations only need one profile within each grid box because the LASE data were already averaged over approximately 37 km.

The highest water vapor mixing ratios produced by RAP were generally in the lowest few hundred meters at night, partially below the minimum range of the lidars. This range limitation omits the lowest one to two vertical levels of RAP from comparison. While these lowest levels should be of general interest for a more complete picture, further examination is beyond the scope of this study.

3. Case overview: 11 July 2015

a. Synoptic environment and LLJ overview

As the LLJ is a nocturnal phenomenon, this case study is focused between sunset at 0200 UTC 11 July and sunrise at 1130 UTC, though we also consider the preceding afternoon. Some of this synoptic overview is taken from RAP fields, which are later shown to have significant errors in moisture and other variables on smaller scales but should be broadly useful for surveying large-scale patterns [the same conditional statement for RAP was made by Peters et al. (2017)]. Johnson et al. (2018) also provided a very brief synoptic overview of this case, showing 0000 UTC data assimilation ensemble fields at different heights.

The 11 July 2015 synoptic setup in the Great Plains was favorable for developing a strong southerly LLJ. The preceding afternoon boundary layer was warm with a southerly geostrophic wind, conducive to both the Blackadar and Holton mechanisms for LLJ development (Blackadar 1957; Holton 1967; Shapiro et al. 2016). A slow-moving warm front had moved northward early in the day to settle along the Kansas–Nebraska border throughout the night (Weather Prediction Center 2015).

Figure 1a shows boundary layer (850 hPa) moisture at sunset. The LLJ began strengthening around sunset, exceeding 20 m s^{-1} by 0600 UTC over most of the region and only weakening slightly by sunrise. Wind direction veered overnight from southerly at sunset to almost westerly at sunrise (Figs. 1a,c show the veering from sunset to 0600 UTC). LLJ winds also veer with height, so the wind directions are more southerly at lower levels than in Fig. 1c. It should also be noted for Fig. 1 that a single pressure level cannot capture the LLJ core across the whole domain; the sloped topography results in different pressure levels for the LLJ core at different locations. While this is objectively a strong LLJ, such events were fairly common during the PECAN time span (Carroll et al. 2019).

Figure 2 shows cross sections of RAP along the transect in Fig. 1b. LLJ wind speeds greater than 12 m s^{-1} were contained below 2 km AGL, also corresponding to the layer of greatest moisture indicative of the daytime PBL depth. Water vapor flux is defined here as the product of the horizontal wind vector magnitude (m s^{-1}) and water vapor mixing ratio (g kg^{-1}), and is revealed in Fig. 2b to generally concentrate below the 310 K isotherm, a consequence of high PBL moisture and the low altitude of the LLJ. To exemplify and contextualize this transport case, a southerly wind speed of 20 m s^{-1} would carry moisture the full meridional distance between FP1 and FP3 in 3.5 h

It should be noted again that the LLJ winds throughout the PECAN domain veer from southerly at sunset (as seen in Fig. 1a) to westerly at sunrise. Although this veer can play an important role in some convection events such as contributing to NCI in the right environments (Gebauer et al. 2018; Smith et al. 2019), details of the LLJ wind veering are less important for describing the mesoscale inflow of this MCS that was already initiated at sundown (Keene and Schumacher 2013). Hence, this study focuses on water vapor flux magnitudes with only brief discussion of wind directions.

b. MCS evolution and reflectivity

A convective system that initiated in the afternoon at 2100 UTC 10 July grew into an MCS overnight, intensifying as it propagated eastward from western Nebraska. It died out in eastern Nebraska between 0800 UTC and sunrise. Another convective system exhibited very similar behavior farther north in Nebraska, though it died out earlier and was not classified as an MCS (Hitchcock et al. 2019). This study focuses on LLJ interaction with the MCS, which was bordered to the south by a region of LLJ-driven moisture convergence throughout its lifetime. Figure 1b shows a snapshot of this; the positive region just north of FP3 indicates moisture convergence at low levels (below 800 hPa, approximately 2 km MSL, encompassing the LLJ depth). The MCS evolved into a "bow-and-arrow" formation (Keene and Schumacher 2013; Weckwerth et al. 2019) with the NCI of the "arrow" branch of cells at 0500–0600 UTC. A bow-and-arrow MCS occurs when quasi-stationary convection (the arrow) occurs above the cold pool behind a preexisting bow echo, often aligned perpendicular to the bow. These events are

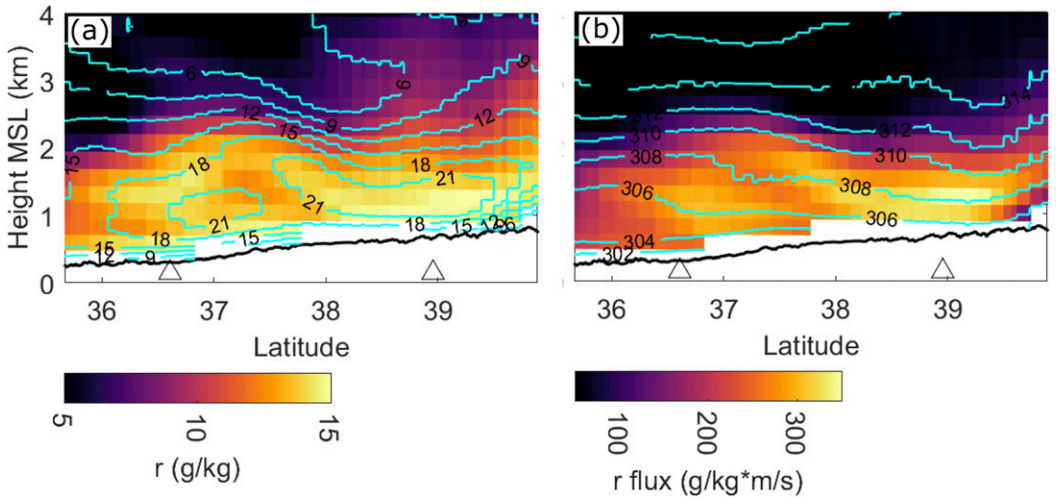

FIG. 2. Cross section of RAP at 0600 UTC along the transect in Fig. 1b, where (a) r is color mapped under wind speed contours (m s^{-1}) and (b) moisture flux under potential temperature contours (K). Triangles indicate FP1 and FP3 locations.

associated with strong southwesterly LLJ inflow of warm moist air and convergence around the cold pool and outflow boundary. Arrows can produce heavy rainfall and severe weather (Keene and Schumacher 2013). Radar observations in Fig. 3 capture the evolution of the MCS and the northern convective system, including the MCS bow-and-arrow at 0600 UTC.

Figure 3d shows the RAP output at 0600 UTC. Comparing the radar observations to modeled composite reflectivity, we see that RAP represents the MCS well. It did not exceed 50 dBZ for the most intense cells, which is likely due to limitations of the 13 km grid size. RAP also overproduced weak reflectivity in patches throughout the domain.

4. Observed and modeled water vapor and winds

a. Ground-based

When combined carefully, lidar observations of moisture and wind from multiple ground sites and an airborne platform provide continuously sampled profiles of the moisture flux across scales. Figure 4 shows the wind and water vapor lidar observations at both ground sites, alongside RAP output for comparison. The southern site FP1 was far upwind of the MCS, well outside the domain of Fig. 3. FP3 was only slightly upwind of the MCS, at the edge of the region of low-level moisture convergence.

Moisture decreased at FP1 as the LLJ strengthened, coincident with a moisture increase at FP3 that was confined to the LLJ core. Although the Raman lidar at FP1 suffered from solar noise before sunset, a radiosonde launched at 2330 UTC reported 16.5 g kg^{-1} water vapor mixing ratio in the PBL. The moist afternoon PBL at FP1 steadily dried by about 4 g kg^{-1} overnight in the residual layer (in and above the LLJ core), whereas the surface-connected inversion layer only dried by about half as much. The relatively dry FP3 afternoon PBL moistened from 13 g kg^{-1} to a maximum of 16 g kg^{-1} within the LLJ core while drying in the residual layer above, especially after 0600 UTC.

The FP1 lidar also resolved a dry layer aloft around 2 km AGL until 0800 UTC, with a minimum measured value of 2.2 g kg^{-1}. The impact of this particular dry layer on convective potential will be explored further in section 5. Such dry layers can also be important to local radiative heating and cloud formation (Deaconu et al. 2019), but further discussion is beyond the scope of this study.

The wind speed at each site evolved in a manner commonly observed in LLJs (e.g., Vanderwende et al. 2015; Klein et al. 2016; Smith et al. 2019) and had very similar maximum speeds, but there were significant differences between the sites. FP1 had faster afternoon wind speeds in the PBL and the LLJ ramped up slowly, reaching maximum speed of 25.0 m s^{-1} around 0800 UTC. In contrast FP3 had slower afternoon PBL speeds that ramped up quickly, reaching max speed of 24.6 m s^{-1} at 0600 UTC. The LLJ profile at FP3 was affected by MCS outflow starting at 0900 UTC, causing slower wind speeds.

While the overall trend of the moisture change at the two sites was captured by RAP, there are clear differences versus the observations in Fig. 4 that are clarified further in Fig. 5. RAP water vapor error fluctuated throughout the night with distinct parcels either too wet or too dry moving over the site, e.g., the 1–2 g kg^{-1} dry bias aloft during the evening transition at both sites (Figs. 5a,b). RAP did not produce the extremely dry layer aloft at FP1.

RAP underpredicted wind speed in the PBL before sunset at FP1 by up to 6 m s^{-1}, then switching after sunset to slight overprediction (up to 3 m s^{-1}) except at the height of LLJ maximum speed (up to 3 m s^{-1} underprediction). At FP3, RAP winds were biased slow in the PBL during the evening transition period (mean bias 1.5 m s^{-1} below 1 km between 2300 and 0200 UTC). RAP produced the LLJ nose well at FP3. Wind direction at the FPs was also modeled well, with a nocturnal mean absolute error below 1 km of 6.6° (not shown). The initial southerly afternoon direction veered with time and height.

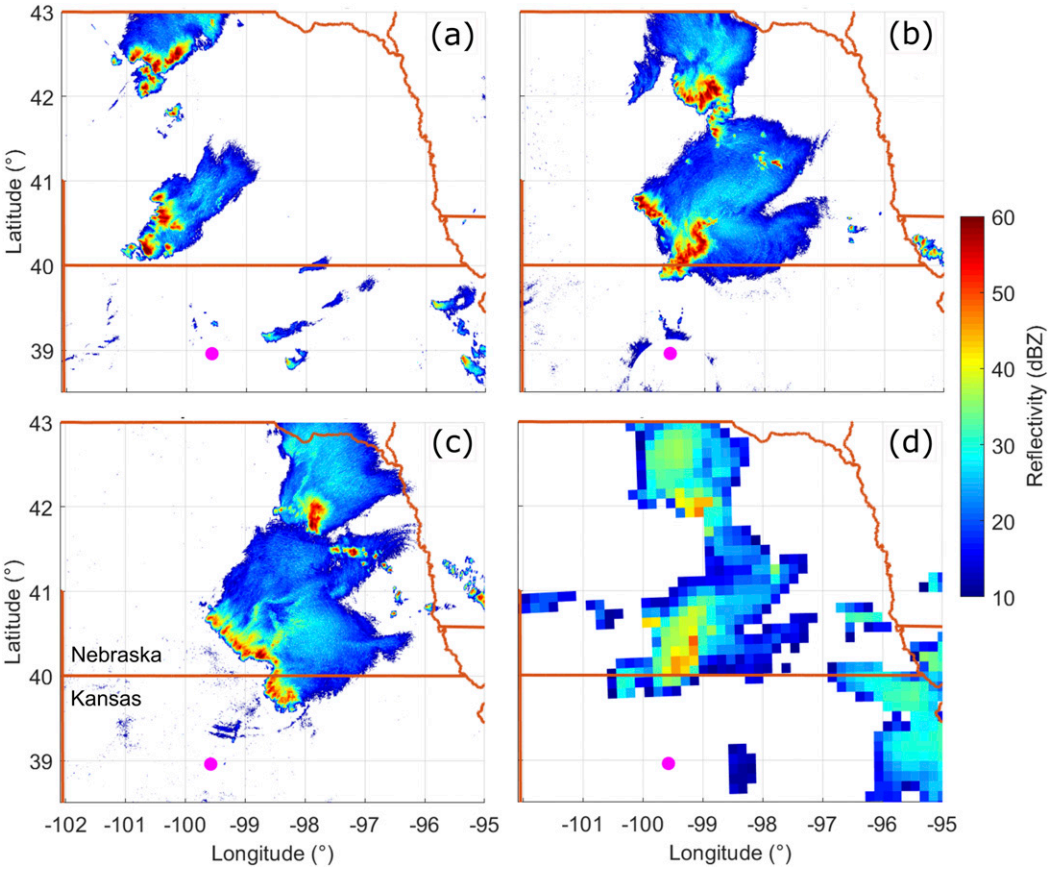

FIG. 3. Radar composite reflectivity observed at (a) 0200, (b) 0600, and (c) 0800 UTC and in the RAP model at (d) 0600 UTC. The domain of these plots corresponds to the dashed box in Fig. 1b. The magenta dot near the bottom of each panel marks FP3 location.

The appendix gives a cursory analysis of the RAP systematic water vapor and wind biases at FP3 over the full PECAN timespan. Biases for this case agree with the systematic errors in approximate timing and signs. Intensive discussion or explanation of the model errors for this case are beyond the scope of this study.

b. *Airborne*

LASE water vapor profiling from onboard the DC-8 spanned much of the domain, revealing mesoscale patterns and some finer-scale features. Figure 6 showcases these data, with pink boxes highlighting some notable regions. Box 1 highlights the southern part of the domain with an overlapping early leg (0200 UTC) showing in the left and right sides of the box and a late leg (0720 UTC) that takes the foreground in the middle of the box. The early leg had a very moist and relatively deep boundary layer, whereas the later leg's water vapor profile was shallow and drier. The highest altitude that had 12 g kg^{-1} or greater moisture fell from 2.3 to 1.8 km and the observed column maximum mixing ratio decreased from 17 to 15 g kg^{-1}.

Box 2 in Fig. 6 captures large moisture content in the eastern half of the PECAN domain up to 3 km MSL, and especially below 1.5 km AGL. This eastern region corresponds to the lowest surface elevations, as the Great Plains terrain slopes downward toward the Mississippi River. In contrast, the higher-elevation far west was very dry, influenced by the dry side of a weak trough present near the Kansas–Colorado border (not shown). Lidar cross sections in Tollerud et al. (2008) also showed a deeper layer of moisture in the east, associated with a deeper boundary layer. Unfortunately, the LASE observations are somewhat limited in their ability to separate spatial differences from temporal evolution as the eastern quarter of the flight domain was only sampled before 0645 UTC and the western quarter only after 0445, without many repeated legs.

A specific example of the benefits of LASE's vertical resolution is presented in Box 3. An elevated moist layer was detected, 700 m deep for most of its length and 2–3 g kg^{-1} wetter than the atmosphere above and below along its length. The moist layer was tilted positively northwest to southeast along the lidar curtain, ranging from 2.0 to 2.8 km AGL. The thin dry layer between the moist PBL and elevated moist layer intruded down as low as 0.8 km AGL. Though mainly within 1–2 km AGL and hence above the LLJ core, this dry layer is still being advected by the LLJ winds that weaken with height up to around 2 km AGL.

Figure 7 visually compares LASE and RAP, with Table 2 presenting comparison statistics. The altitude layers in Table 2

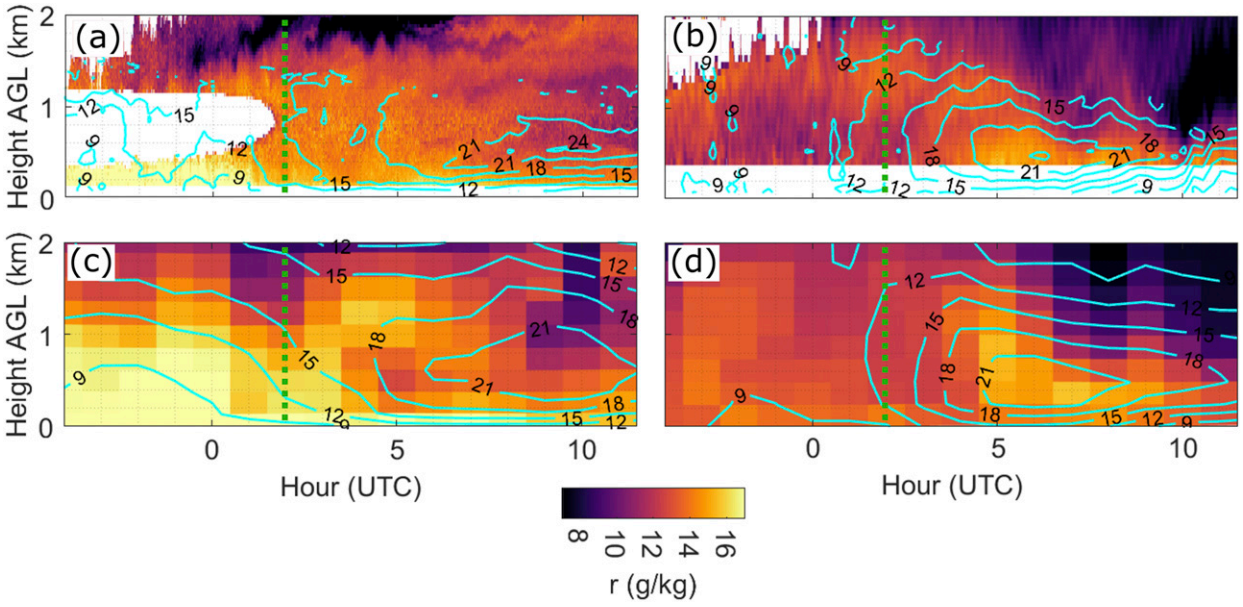

FIG. 4. Time–height cross sections of r (color) and wind speed (contours, m s^{-1}) at (a),(c) FP1 and (b),(d) FP3 from 2000 UTC 10 Jul to 1130 UTC 11 Jul (sunrise). Lidar observations are in (a),(b) and RAP observations are in (c),(d). Lidar observations have limited range; lack of data are white for r, and for winds data are absent above the broken contours in the 1–2 km range. Dashed green lines mark sunset (0200 UTC).

roughly correspond to the PBL (0–2.5 km), midlevels (2.5–5 km), and dry upper levels (5–8 km) over the domain. Interpretation of the Table 2 statistics must be done carefully due to the naturally wide range of r as well as the limited spatial and temporal sampling. The largest RMSE is in the lowest layer, though this is expected because the values of r are largest in the lowest layer. The uppermost altitude range has the worst accuracy as represented by correlation coefficient (R^2), but this layer is dry enough for the RMSE to remain low.

As with the ground-based lidar comparisons, RAP captured general patterns but had inaccuracies in water vapor mixing ratio, typically with contiguous regions that were too wet or too dry, and occasionally exceeded 2 g kg^{-1} difference from LASE. Regarding spatial distribution (e.g., Fig. 7), notable RAP errors include excessive PBL moisture over eastern KS (a 1.4 g kg^{-1} mean moist bias below 2 km, east of −98° longitude), and in the southwest RAP was drier than LASE during both an early and a late flight leg (a 1.0 g kg^{-1} mean dry bias below 5 km, west of −100° longitude and south of 39° latitude). RAP did not produce the dry and moist layering of Fig. 6 Box 3.

5. Moisture flux and impact on convective potential

Now that the ground-based and airborne lidar observations have been shown and discussed independently, an analysis of moisture flux (defined as the product of the previously examined r and horizontal wind speed) will be presented, also tying in parameters of convective potential and evolution of the MCS. Moisture flux calculation is limited to the ground sites with both Doppler and water vapor lidars.

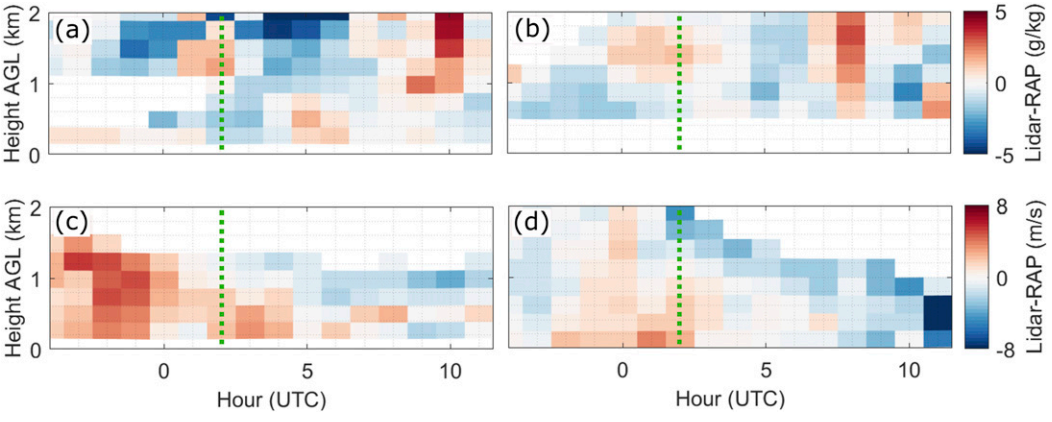

FIG. 5. Differences between the lidar observations and RAP output fields from Fig. 4. (a),(b) Water vapor and (c),(d) wind at (a),(c) FP1 and (b),(d) FP3. Differences are defined as observations − model. Green dashed lines mark sunset.

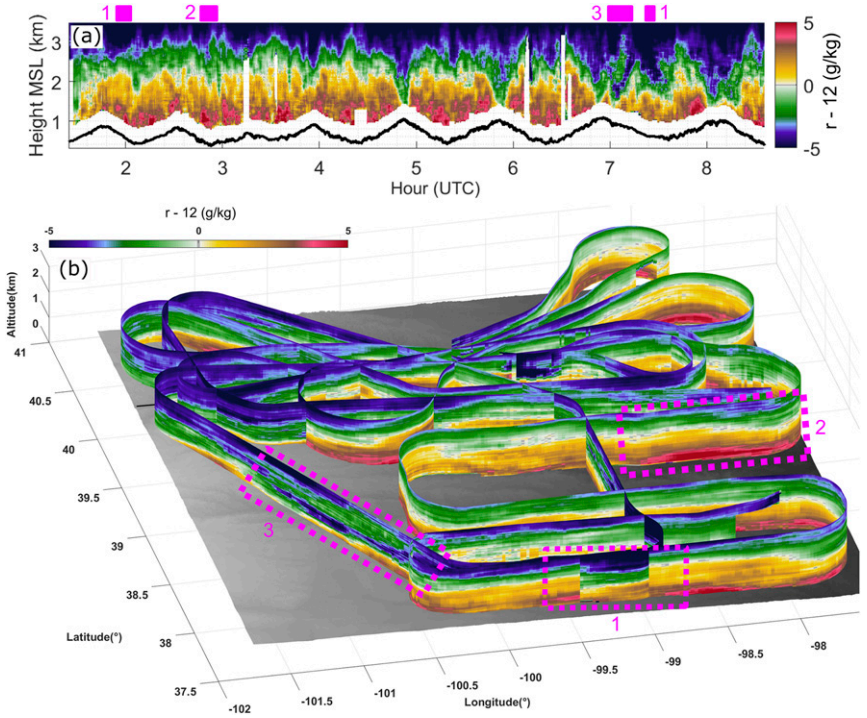

FIG. 6. LASE data (a) below 3.5 km and (b) below 3 km MSL. The values shown are $r - 12\,\mathrm{g\,kg^{-1}}$. This subtraction of the approximate mean r is done to emphasize spatiotemporal differences. Sections marked in pink are discussed in the text. The gray-shaded underlying field is terrain height.

Figure 8 shows plots of the measured water vapor flux, revealing very different profile evolutions at the two FPs. The FP1 lidars observed relatively constant moisture flux throughout the night, with a gradual ramp-up from afternoon to the LLJ core around 0700 UTC, and only slight variation vertically within the PBL. The picture at FP3 is a sharp contrast, with relatively low evening values that ramp up very quickly, reaching maximum at 0430 UTC. This maximum is compact in altitude around the LLJ core at 450 m AGL, and persists until around 0900 UTC, at which point the LLJ at the site is being influenced by MCS outflow (especially below 500 m AGL). Overall a large-scale moisture flux from south to north is apparent, with smaller features caused by the sites' unique LLJ and moisture structures and timings. RAP produced the large-scale trends well.

The FP3 maximum water vapor flux was coincident with a large branch of NCI in the MCS at the Kansas–Nebraska border. At 0500 UTC, shortly after the flux reached its maximum at 0430 UTC, NCI occurred behind the MCS that

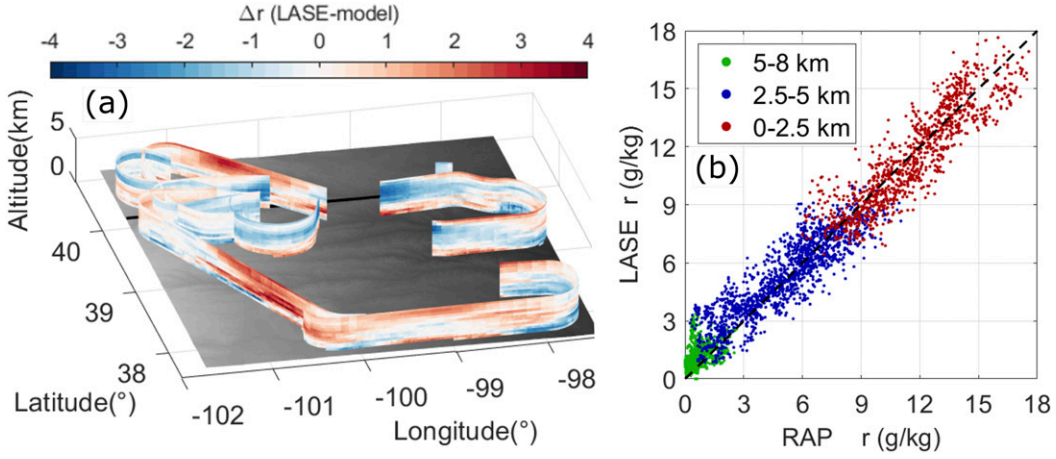

FIG. 7. (b) LASE vs RAP r scatterplot for 0–8 km MSL and (a) the associated difference curtain from 0 to 5 km MSL. The curtain in (a) is sparser than Fig. 6 due to the filtering outlined in section 2d.

TABLE 2. Linear regression statistics for the LASE vs RAP mixing ratio scatterplots in Fig. 7. Bias is calculated as LASE − model.

Altitude range (km MSL)	Bias (g kg^{-1})	RMSE (g kg^{-1})	R^2
0–8	0.18	0.94	0.96
0–2.5	−0.14	1.14	0.79
2.5–5	0.18	0.97	0.81
5–8	0.46	0.63	0.35

intensified over the course of an hour to produce the ''arrow'' in Fig. 3b, then becoming the extended line of Fig. 3c.

Figure 9 provides a quantitative look at the evolution of CAPE and CIN for this case, calculated both far and near upwind of the MCS from radiosondes at FP1 and FP3, respectively [values reported from UCAR/NCAR–EOL (2016c)]. Surface CAPE at FP1 decreased rapidly after sunset until sunrise, whereas FP3 only had a weak minimum at sunset with little change over the course of the night. Surface CIN increased steadily at the same rate at both sites, likely due to the near-surface cooling as the nocturnal inversion developed. The most unstable parcel (MUP) CAPE trends differed between FP1, where it decreased almost as much as the surface CAPE, versus at FP3, which again had a weak minimum at sunset but then grew to a maximum of 2842 J kg^{-1} by 0600 UTC. The MUP after sunset at FP3 stayed between 400 and 750 m AGL; above the strong surface-connected inversion and in the LLJ core. The MUP at FP1 overnight was just above the surface-connected inversion layer, at 250 m AGL, below the core of maximum LLJ winds (as determined by the 0527 UTC radiosonde profile).

There was an enhancement of CAPE aloft (especially in the LLJ core depth) in the north, just upwind of the MCS, and a sharp decrease in CAPE at all altitudes to the far south. The FP3 CAPE maximum coincided temporally and vertically with the maximum LLJ water vapor flux as well as the NCI and intensification of the ''arrow'' of the MCS.

To further investigate the contributions of the LLJ to convective potential, Fig. 10 shows the change in moist static energy (MSE) at the two sites over 6 h, from 2 h before sunset to 4 h after sunset, calculated from radiosonde profiles. The change in MSE at a given altitude is $\Delta\text{MSE} = \text{MSE}_2 - \text{MSE}_1 = C_p(T_2 - T_1) + L_v(r_2 - r_1)$, where C_p is the specific heat of air at constant pressure, L_v is the latent heat of water vaporization, and the subscripts 1 and 2 refer to early and late radiosonde launches, respectively. The terms of ΔMSE are also plotted separately to examine behavior of individual components, similar to Peters et al. (2017). The temperature and moisture contributions are $\Delta\text{MSE}_T = C_p(T_2 - T_1)$ and $\Delta\text{MSE}_r = L_v(r_2 - r_1)$, respectively.

All six curves in Fig. 10 are approximately zero near 1 km AGL. Below this altitude, the LLJ is expected to play a major role in the observed changes. Higher altitudes still experienced southeasterly synoptic winds, but had less influence from the LLJ or other PBL processes. At FP1, the PBL drying discussed

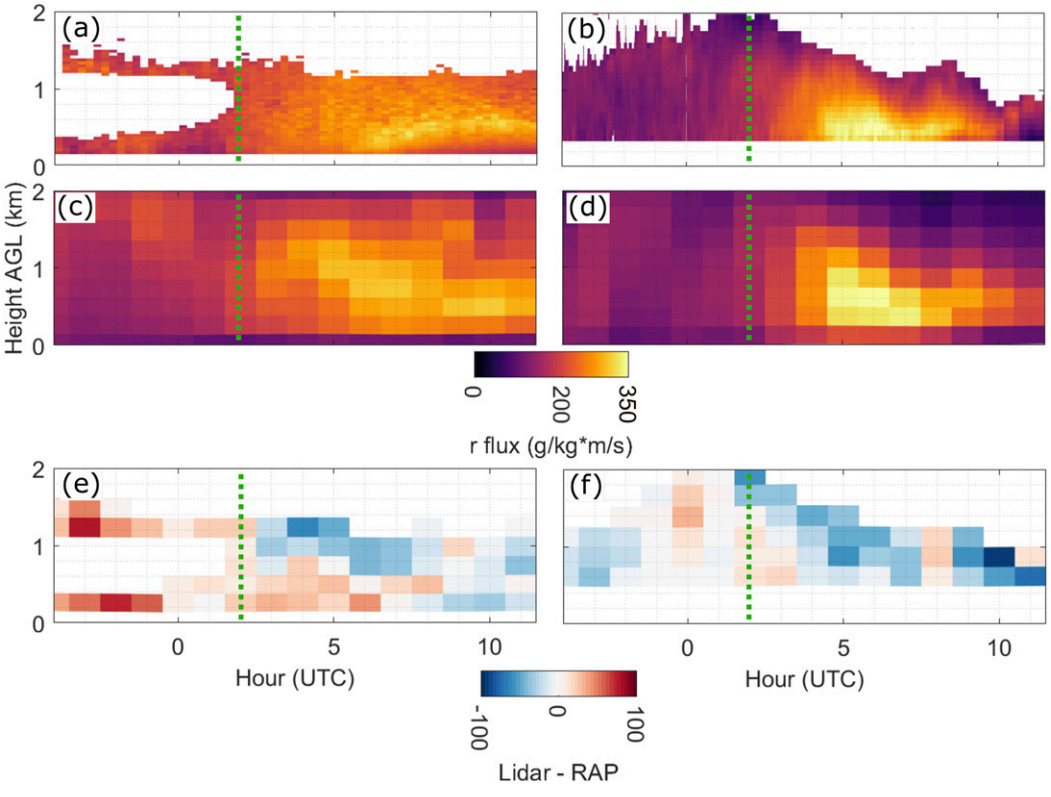

FIG. 8. (a),(c),(e) FP1 and (b),(d),(f) FP3 moisture flux from (a),(b) lidars; (c),(d) RAP; and (e),(f) the lidar − model difference using the same time and height axes as in Fig. 4. Green dashed lines mark sunset.

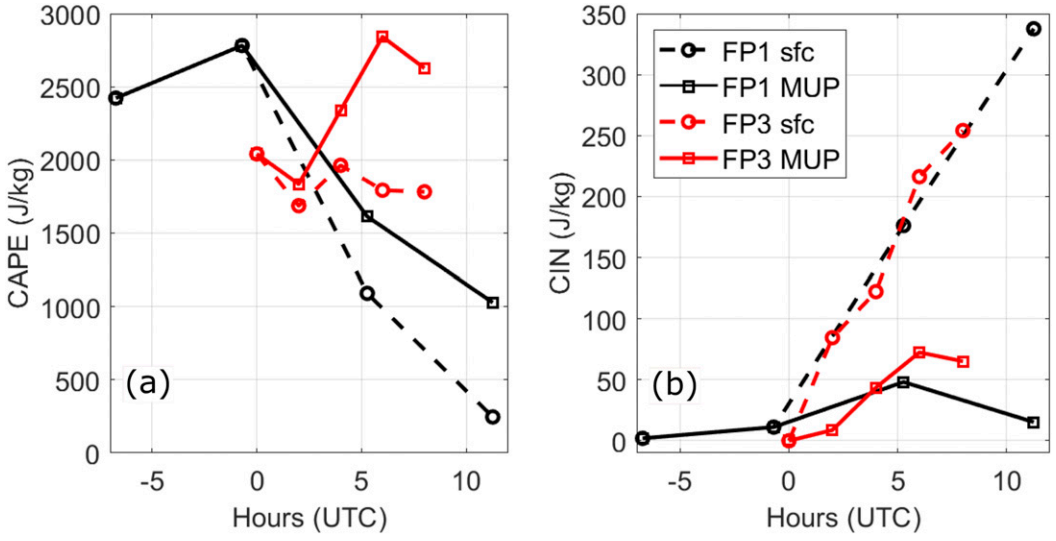

FIG. 9. (a) CAPE and (b) CIN for surface (sfc) and MUP at FP1 and FP3 from afternoon through sunrise, calculated from radiosonde profiles. The "0" on the horizontal axis indicates 0000 UTC 11 Jul 2015.

earlier was apparent in ΔMSE_r, and ΔMSE_T showed little change in temperature above the surface-connected nocturnal inversion. The largest peak and trough in ΔMSE_r at FP1, between 1.4 and 2.5 km, were caused by the very dry layer discussed in section 4a being observed at a higher altitude during the second radiosonde launch. At FP3, MSE_r increased by up to 7.2 kJ kg^{-1} below 1 km. The FP3 MSE_T below 1 km evolved in such a way as to oppose that increasing MSE_r. This resulted in net ΔMSE of nearly zero except in the LLJ core, between the surface-connected inversion top (0.3 km) and 0.9 km, where increasing moisture dominated for a maximum ΔMSE of 5.0 kJ kg^{-1}.

These measurements suggest that FP3′s increased convective potential at low levels was enhanced by the moisture increase and that the convective potential was actually inhibited by temperature change. This situation reverses above 1 km AGL, but with ΔMSE_r still controlling the sign of ΔMSE. The LLJ has often been cited for its advection of warm temperatures contributing to growth of convective potential (e.g., Trier and Parsons 1993; Peters and Schumacher 2016), but this was not necessarily true for this case.

It should also be noted that while the LLJ does play a major role below 2 km, especially the lowest 1 km, other effects including radiative cooling at night and surface exchange of moisture impact ΔMSE but quantification of their relative influences is not possible here. For example, temperature advection by the LLJ may have sustained warmer temperatures than would have otherwise occurred under the sole influence of radiative cooling. There are also other factors in play affecting convection, such as the previously discussed wind field convergence.

6. Summary and discussion

This manuscript has presented case study observations of southerly moisture transport across the Great Plains by an LLJ, using ground-based and airborne water vapor and wind lidars to resolve important features across scales. Measurements showed an overall trend of northward moisture flux. At the northern site (FP3) the water vapor mixing ratio increase of 3 g kg^{-1} was predominantly confined to the lowest kilometer, especially in the LLJ core around 400–700 m, despite the late afternoon moist boundary layer extending up to 2 km. A water vapor mixing ratio decrease of 4 g kg^{-1} was observed in the southern (FP1) boundary layer.

This case featured an MCS downwind of the ground sites that initiated in the afternoon and was sustained until around sunrise. A large branch of NCI began and intensified coincident with the

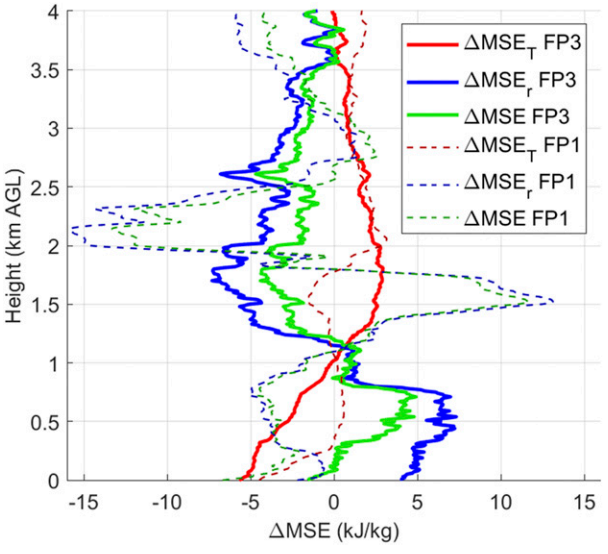

FIG. 10. Temporal change in MSE and components at FP1 (dashed lines) and FP3 (solid lines) calculated from radiosonde observations. Launch times at FP1 were 2330 and 0527 UTC, and at FP3 were 0000 and 0600 UTC.

maximum observed moisture flux at FP3, resulting in a bow-and-arrow MCS structure. In the RAP analysis, there was a region of positive moisture convergence below 800 hPa all night on the upwind LLJ side (i.e., south) of the MCS.

The impact of the mesoscale moisture transport on convective potential was explored using CAPE, CIN, and MSE calculated from radiosondes. CAPE dropped dramatically in the south for both surface and MUPs. At the northern site CAPE was at a minimum at sunset then increased aloft overnight, with the MUP in the LLJ core at the time of maximum moisture flux. Temporal changes in MSE reinforced the mesoscale transport narrative, and changes were dominated by moisture rather than temperature. At FP1, a very dry layer above the PBL had a strong impact on ΔMSE_r.

The lidar observations of water vapor mixing ratio and wind were compared to the operational RAP model analysis. RAP was found to have mixing ratio errors up to and occasionally exceeding $2\,g\,kg^{-1}$, though comparison with airborne water vapor lidar data below 2.5 km MSL gave a wet bias of only $0.14\,g\,kg^{-1}$ with $1.14\,g\,kg^{-1}$ RMSE. The RAP errors mostly manifested as contiguous dry or wet regions ranging from dozens of km up to 200 km in scale. This included failure to produce smaller-scale features that the lidars captured, including very dry layers in the lowest 2.5 km of the atmosphere, most likely due to the inadequacy of the observations used in the analysis (e.g., surface-based METAR and airborne-based AMDAR) to observe these features. Assimilating high-temporal-resolution observations from a distributed network of ground-based thermodynamic profilers has been shown to provide improved analyses and lead to better forecasts of a range of meteorological events (e.g., Hu et al. 2019; Degelia et al. 2020).

This research has improved our understanding of LLJ moisture transport and its connections to convection and convective potential. The unprecedented detail and coverage of the lidar observations surpasses the only other lidar-based LLJ moisture transport study in the literature (Tollerud et al. 2008), and the direct ties to an MCS and NCI in this case are aligned with the PECAN campaign research questions. Comparison to RAP analysis identified the structure and magnitude of model water vapor errors in the domain, and this knowledge can potentially be applied to inform RAP usage in meteorological studies or future efforts toward model improvements. While this study was limited in scope of model analysis, more in-depth model comparisons could benefit from characterizing model spatial variability, and from assessing model forecasts.

These intensive lidar observations of moisture and wind have yielded a great breadth of information for this case study, but much more can be gained from continued lidar research on these topics. Performing similar studies from the PECAN datasets is possible, and future experiments and observational networks could benefit from emphasizing such lidar synergy. In addition, profiling temperature via lidar or other remote sensors would be valuable for generating time series profiles of convective potential and other thermodynamic metrics (e.g., Wagner et al. 2008; Blumberg et al. 2017).

Acknowledgments. This work was funded by National Science Foundation Award AGS-1503563 to the University of Maryland, Baltimore County, and by the National Aeronautics and Space Administration Minority University Research and Education Project (NASA-MUREP) IRO NNX15AQ03A. Belay Demoz and Ruben Delgado were also partially funded by the National Oceanic and Atmospheric Administration–Cooperative Science Center for Atmospheric Sciences and Meteorology (NOAA-NCAS-M) and Center for Earth System Sciences and Remote Sensing Technologies (NOAA-CESSRST) under the Cooperative Agreement Grants NA16SEC4810006 and NA16SEC4810008, respectively. Thanks to Richard Ferrare and Susan Kooi for helping to interpret LASE data, and to Stacey Hitchcock and Russ Schumacher for providing radiosonde CAPE and CIN values. Additional thanks to all fellow PECAN participants.

Data availability statement. All observational datasets used for this research are in the PECAN archive managed by NCAR/EOL under the sponsorship of the National Science Foundation, https://data.eol.ucar.edu/master_list/?project=PECAN. Citations for the specific datasets are referenced in the text. RAP model data for this case was not publicly archived when acquired for this research, but may be obtained via the authors.

APPENDIX

RAP Biases at FP3 for the Full PECAN Time Span

It is important to compare systematic model behavior to the performance of this specific case. To improve understanding in this regard, a cursory analysis is presented here of the full PECAN timespan of water vapor and wind biases at FP3.

The water vapor plots shown in the Appendix use FP3 Atmospheric Emitted Radiance Interferometer (AERI) data, where the FP3 water vapor lidar data has been incorporated into the AERI optimal estimation (AERIoe) retrieval (as in Turner and Blumberg 2019; Turner and Lohnert (2020, manuscript submitted to *Atmos. Meas. Tech.*). AERI is a passive remote sensor that measures downwelling radiation to retrieve thermodynamic profiles, and is a popular tool in atmospheric research (Knuteson et al. 2004a,b; Turner and Löhnert 2014). The AERI data provides observations from the surface upward, also incorporating FP3 water vapor lidar information. The AERIoe was used here instead of the lidar alone because the AERI had better coverage over the entire PECAN campaign. Because of the good signal-to-noise ratio, the DIAL's water vapor observations are largely unchanged during the retrieval process, but the combined retrieval provides data both below and above the DIAL's normal data availability and range.

Figures A1 and A2 show plots of average biases for r and wind speed over the whole PECAN timespan at FP3, subtracting observations from models. The observations came from the FP3 Doppler lidar (wind) and AERI (r via AERIoe). The plots show that the 11 July 2015 biases of water vapor and wind at FP3 agree qualitatively with most features of the full campaign average biases. There are apparent differences and

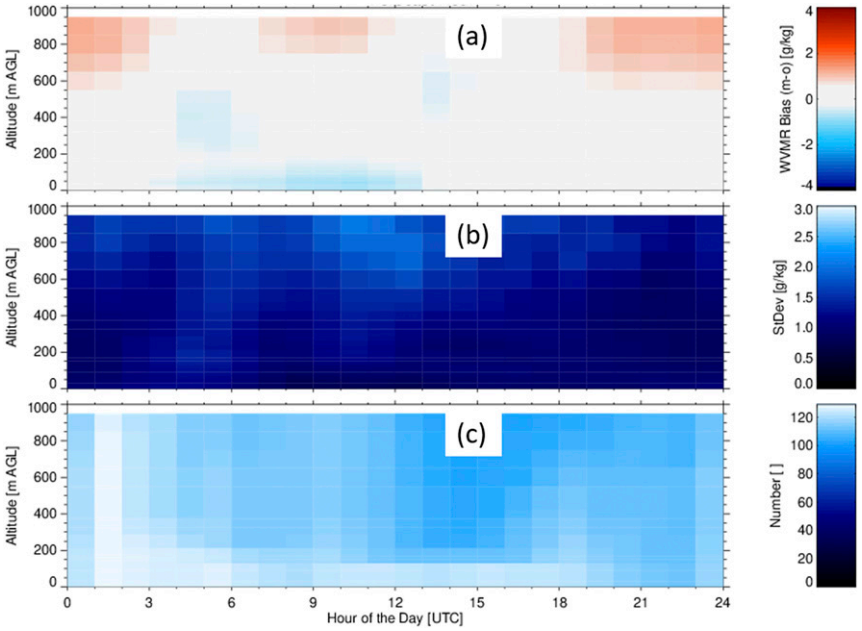

FIG. A1. RAP vs AERIoe PECAN (a) average r bias, (b) error standard deviation, and (c) number of comparisons at each point at FP3.

relatively finescale features in the 11 July case, but overall it mimics much of the systematic model behavior.

RAP was systematically too moist at most hours in the 0.8–1.0 km layer by up to 1.0 g kg^{-1}, similar to the case study. Below 150 m there was a slight dry bias (<1 g kg^{-1}) overnight that was not present during the day, but this is below the minimum range of the FP3 water vapor lidar comparison. For wind speeds, RAP average bias was small (<2.5 m s^{-1}) at all hours, with a consistent fast bias for most of the night and the morning transition (0400–1300 UTC). As with the water vapor, the wind speed case study errors are qualitatively comparable to the full-campaign biases in timing and sign.

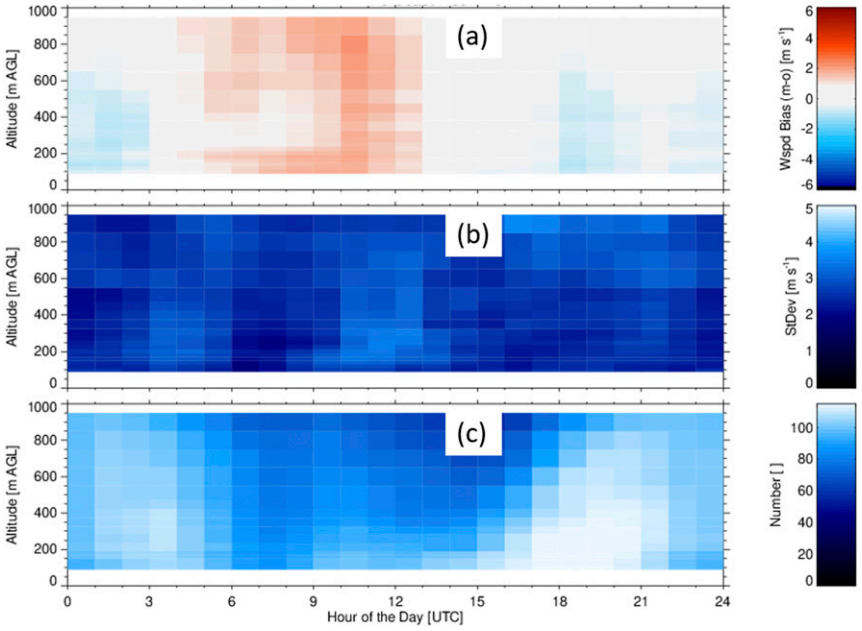

FIG. A2. RAP vs Doppler lidar PECAN (a) average wind speed bias, (b) error standard deviation, and (c) number of comparisons at each point at FP3.

REFERENCES

ARM Data Center, 2014: Doppler Lidar (sgpdlprofwind4newsC1) 2015-07-10 to 2015-07-11, Southern Great Plains (SGP) Central Facility, Lamont, OK (C1). Atmospheric Radiation Measurement (ARM) Data Center, accessed 21 May 2018, https://doi.org/10.5439/1374838.

——, 2015: Raman Lidar (sgp10srlprofmr1turnC1) 2015-07-10 to 2015-07-11, Southern Great Plains (SGP) Central Facility, Lamont, OK (C1). Atmospheric Radiation Measurement (ARM) Data Center, accessed 26 July 2018, https://www.arm.gov/capabilities/observatories/sgp/locations/c1.

Augustine, J. A., and F. Caracena, 1994: Lower-tropospheric precursors to nocturnal MCS development over the central United States. *Wea. Forecasting*, **9**, 116–135, https://doi.org/10.1175/1520-0434(1994)009<0116:LTPTNM>2.0.CO;2.

Benjamin, S. G., and Coauthors, 2016: A North American hourly assimilation and model forecast cycle: The Rapid Refresh. *Mon. Wea. Rev.*, **144**, 1669–1694, https://doi.org/10.1175/MWR-D-15-0242.1.

Berg, L. K., L. D. Riihimaki, Y. Qian, H. Yan, and M. Huang, 2015: The low-level jet over the Southern Great Plains determined from observations and reanalyses and its impact on moisture transport. *J. Climate*, **28**, 6682–6706, https://doi.org/10.1175/JCLI-D-14-00719.1.

Bergmaier, P. T., B. Geerts, Z. Wang, B. Liu, and P. C. Campbell, 2014: A dryline in southeast Wyoming. Part II: Airborne in situ and Raman lidar observations. *Mon. Wea. Rev.*, **142**, 2961–2977, https://doi.org/10.1175/MWR-D-13-00314.1.

Blackadar, A. K., 1957: Boundary layer wind maxima and their significance for the growth of nocturnal inversions. *Bull. Amer. Meteor. Soc.*, **38**, 283–290, https://doi.org/10.1175/1520-0477-38.5.283.

Blumberg, W. G., T. J. Wagner, D. D. Turner, and J. Correia, 2017: Quantifying the accuracy and uncertainty of diurnal thermodynamic profiles and convection indices derived from the atmospheric emitted radiance interferometer. *J. Appl. Meteor. Climatol.*, **56**, 2747–2766, https://doi.org/10.1175/JAMC-D-17-0036.1.

Bonin, T. A., W. G. Blumberg, P. M. Klein, and P. B. Chilson, 2015: Thermodynamic and turbulence characteristics of the Southern Great Plains nocturnal boundary layer under differing turbulent regimes. *Bound.-Layer Meteor.*, **157**, 401–420, https://doi.org/10.1007/s10546-015-0072-2.

Bonner, W. D., 1968: Climatology of the low level jet. *Mon. Wea. Rev.*, **96**, 833–850, https://doi.org/10.1175/1520-0493(1968)096<0833:COTLLJ>2.0.CO;2.

Browell, E. V., and Coauthors, 1997: LASE Validation Experiment. *Advances in Atmospheric Remote Sensing with Lidar*, A. Ansmann et al., Eds., Springer, 289–295, https://doi.org/10.1007/978-3-642-60612-0_70.

Byerle, L., and J. Paegle, 2003: Modulation of the Great Plains low-level jet and moisture transports by orography and large-scale circulations. *J. Geophys. Res.*, **108**, 8611, https://doi.org/10.1029/2002JD003005.

Carroll, B. J., B. B. Demoz, and R. Delgado, 2019: An overview of low-level jet winds and corresponding mixed layer depths during PECAN. *J. Geophys. Res.*, **124**, 9141–9160, https://doi.org/10.1029/2019JD030658.

Clark, R., 2016: FP3 Ellis, KS radiosonde data, version 2.0. UCAR/NCAR–Earth Observing Laboratory, accessed 9 February 2019, https://doi.org/10.5065/D6GM85DZ.

Deaconu, L. T., N. Ferlay, F. Waquet, F. Peers, F. Thieuleux, and P. Goloub, 2019: Satellite inference of water vapour and above-cloud aerosol combined effect on radiative budget and cloud-Top processes in the southeastern Atlantic Ocean. *Atmos. Chem. Phys.*, **19**, 11 613–11 634, https://doi.org/10.5194/acp-19-11613-2019.

Degelia, S. K., X. Wang, and D. J. Stensrud, 2019: An evaluation of the impact of assimilating AERI retrievals, kinematic profilers, rawinsondes, and surface observations on a forecast of a nocturnal convection initiation event during the PECAN field campaign. *Mon. Wea. Rev.*, **147**, 2739–2764, https://doi.org/10.1175/MWR-D-18-0423.1.

——, ——, ——, and D. D. Turner, 2020: Systematic evaluation of the impact of assimilating a network of ground-based remote sensing profilers for forecasts of nocturnal convection initiation during PECAN. *Mon. Wea. Rev.*, **148**, 4703–4728, https://doi.org/10.1175/MWR-D-20-0118.1.

Doubler, D. L., J. A. Winkler, X. Bian, C. K. Walters, and S. Zhong, 2015: An NARR-derived climatology of southerly and northerly low-level jets over North America and coastal environs. *J. Appl. Meteor. Climatol.*, **54**, 1596–1619, https://doi.org/10.1175/JAMC-D-14-0311.1.

Du, Y., and R. Rotunno, 2014: A simple analytical model of the nocturnal low-level jet over the Great Plains of the United States. *J. Atmos. Sci.*, **71**, 3674–3683, https://doi.org/10.1175/JAS-D-14-0060.1.

Ferrare, R., A. Nehrir, S. Kooi, C. Butler, and A. Notari, 2016: NASA DC-8 LASE data, version 1.0. UCAR/NCAR–Earth Observing Laboratory, accessed 20 July 2018, https://doi.org/10.5065/D69C6VM6.

Gebauer, J. G., A. Shapiro, E. Fedorovich, and P. Klein, 2018: Convection initiation caused by heterogeneous low-level jets over the Great Plains. *Mon. Wea. Rev.*, **146**, 2615–2637, https://doi.org/10.1175/MWR-D-18-0002.1.

Geerts, B., and Coauthors, 2017: The 2015 Plains Elevated Convection At Night Field Project. *Bull. Amer. Meteor. Soc.*, **98**, 767–786, https://doi.org/10.1175/BAMS-D-15-00257.1.

Grasmick, C., B. Geerts, D. D. Turner, Z. Wang, and T. M. Weckwerth, 2018: The relation between nocturnal MCS evolution and its outflow boundaries in the stable boundary layer: An observational study of the 15 July 2015 MCS in PECAN. *Mon. Wea. Rev.*, **146**, 3203–3226, https://doi.org/10.1175/MWR-D-18-0169.1.

Hanesiak, J., and D. Turner, 2016: FP3 University of Manitoba Doppler Lidar Wind Profile Data, version 1.0. UCAR/NCAR–Earth Observing Laboratory, accessed 30 May 2017, https://doi.org/10.5065/D60863P5.

Higgins, R. W., Y. Yao, E. S. Yarosh, J. E. Janowiak, and K. C. Mo, 1997: Influence of the Great Plains low-level jet on summertime precipitation and moisture transport over the central United States. *J. Climate*, **10**, 481–507, https://doi.org/10.1175/1520-0442(1997)010<0481:IOTGPL>2.0.CO;2.

Hitchcock, S. M., R. S. Schumacher, G. R. Herman, M. C. Coniglio, M. D. Parker, and C. L. Ziegler, 2019: Evolution of pre- and postconvective environmental profiles from mesoscale convective systems during PECAN. *Mon. Wea. Rev.*, **147**, 2329–2354, https://doi.org/10.1175/MWR-D-18-0231.1.

Holton, J. R., 1967: The diurnal boundary layer wind oscillation above sloping terrain. *Tellus*, **19**, 199–205, https://doi.org/10.1111/j.2153-3490.1967.tb01473.x.

Hu, J., N. Yussouf, D. D. Turner, T. A. Jones, and X. Wang, 2019: Impact of ground-based remote sensing boundary layer observations on short-term probabilistic forecasts of a tornadic supercell event. *Wea. Forecasting*, **34**, 1453–1476, https://doi.org/10.1175/WAF-D-18-0200.1.

Johnson, A., X. Wang, K. R. Haghi, and D. B. Parsons, 2018: Evaluation of forecasts of a convectively generated bore using an intensively observed case study from PECAN. *Mon. Wea. Rev.*, **146**, 3097–3122, https://doi.org/10.1175/MWR-D-18-0059.1.

Kahn, B. H., and Coauthors, 2011: Temperature and water vapor variance scaling in global models: Comparisons to satellite and aircraft data. *J. Atmos. Sci.*, **68**, 2156–2168, https://doi.org/10.1175/2011JAS3737.1.

Keene, K. M., and R. S. Schumacher, 2013: The bow and arrow mesoscale convective structure. *Mon. Wea. Rev.*, **141**, 1648–1672, https://doi.org/10.1175/MWR-D-12-00172.1.

Klein, P. M., X. M. Hu, A. Shapiro, and M. Xue, 2016: Linkages between boundary-layer structure and the development of nocturnal low-level jets in central Oklahoma. *Bound.-Layer Meteor.*, **158**, 383–408, https://doi.org/10.1007/s10546-015-0097-6.

Knuteson, R. O., and Coauthors, 2004a: Atmospheric Emitted Radiance Interferometer. Part I: Instrument design. *J. Atmos. Oceanic Technol.*, **21**, 1763–1776, https://doi.org/10.1175/JTECH-1662.1.

——, and Coauthors, 2004b: Atmospheric Emitted Radiance Interferometer. Part II: Instrument performance. *J. Atmos. Oceanic Technol.*, **21**, 1777–1789, https://doi.org/10.1175/JTECH-1663.1.

Koch, S. E., C. Flamat, J. W. Wilson, B. M. Gentry, and B. D. Jamison, 2008: An atmospheric soliton observed with Doppler radar, differential absorption lidar, and a molecular Doppler lidar. *J. Atmos. Oceanic Technol.*, **25**, 1267–1287, https://doi.org/10.1175/2007JTECHA951.1.

Lin, G., B. Geerts, Z. Wang, C. Grasmick, X. Jing, and J. Yang, 2019: Interactions between a nocturnal MCS and the stable boundary layer, as observed by an airborne compact Raman lidar during PECAN. *Mon. Wea. Rev.*, **147**, 3169–3189, https://doi.org/10.1175/MWR-D-18-0388.1.

Markowski, P., and Y. Richardson, 2010: *Mesoscale Meteorology in Midlatitudes*. John Wiley and Sons, 430 pp.

Peters, J. M., and R. S. Schumacher, 2016: Dynamics governing a simulated mesoscale convective system with a training convective line. *J. Atmos. Sci.*, **73**, 2643–2664, https://doi.org/10.1175/JAS-D-15-0199.1.

——, E. R. Nielsen, M. D. Parker, S. M. Hitchcock, and R. S. Schumacher, 2017: The impact of low-level moisture errors on model forecasts of an MCS observed during PECAN. *Mon. Wea. Rev.*, **145**, 3599–3624, https://doi.org/10.1175/MWR-D-16-0296.1.

Pu, B., and R. E. Dickinson, 2014: Diurnal spatial variability of Great Plains summer precipitation related to the dynamics of the low-level jet. *J. Atmos. Sci.*, **71**, 1807–1817, https://doi.org/10.1175/JAS-D-13-0243.1.

Reif, D. W., and H. B. Bluestein, 2018: Initiation mechanisms of nocturnal convection without nearby surface boundaries over the central and Southern Great Plains during the warm season. *Mon. Wea. Rev.*, **146**, 3053–3078, https://doi.org/10.1175/MWR-D-18-0040.1.

Schäfler, A., A. Dörnbrack, C. Kiemle, S. Rahm, and M. Wirth, 2010: Tropospheric water vapor transport as determined from airborne lidar measurements. *J. Atmos. Oceanic Technol.*, **27**, 2017–2030, https://doi.org/10.1175/2010JTECHA1418.1.

Schumacher, R. S., 2015: Resolution dependence of initiation and upscale growth of deep convection in convection-allowing forecasts of the 31 May–1 June 2013 supercell and MCS. *Mon. Wea. Rev.*, **143**, 4331–4354, https://doi.org/10.1175/MWR-D-15-0179.1.

Shapiro, A., E. Federovich, and S. Rahimi, 2016: A unified theory for the Great Plains nocturnal low-level jet. *J. Atmos. Sci.*, **73**, 3037–3057, https://doi.org/10.1175/JAS-D-15-0307.1.

Sisterson, D. L., R. A. Peppler, T. S. Cress, P. J. Lamb, and D. D. Turner, 2016: The ARM Southern Great Plains (SGP) site. *The Atmospheric Radiation Measurement Program: The First 20 Years, Meteor. Monogr.*, No. 57, Amer. Meteor. Soc., https://doi.org/10.1175/AMSMONOGRAPHS-D-16-0004.1.

Smith, E. N., J. A. Gibbs, E. Fedorovich, and P. M. Klein, 2018: WRF Model study of the Great Plains low-level jet: Effects of grid spacing and boundary layer parameterization. *J. Appl. Meteor. Climatol.*, **57**, 2375–2397, https://doi.org/10.1175/JAMC-D-17-0361.1.

——, J. G. Gebauer, P. M. Klein, E. Fedorovich, and J. A. Gibbs, 2019: The Great Plains low-level jet during PECAN: Observed and simulated characteristics. *Mon. Wea. Rev.*, **147**, 1845–1869, https://doi.org/10.1175/MWR-D-18-0293.1.

Song, J., K. Liao, R. L. Coulter, and B. M. Lesht, 2005: Climatology of the low-level jet at the southern Great Plains atmospheric boundary layer experiments site. *J. Appl. Meteor.*, **44**, 1593–1606, https://doi.org/10.1175/JAM2294.1.

Spuler, S. M., K. S. Repasky, B. Morley, D. Moen, M. Hayman, and A. R. Nehrir, 2015: Field-deployable diode-laser-based differential absorption lidar (DIAL) for profiling water vapor. *Atmos. Meas. Tech.*, **8**, 1073–1087, https://doi.org/10.5194/amt-8-1073-2015.

Steinke, S., S. Eikenberg, U. Löhnert, G. Dick, D. Klocke, P. Di Girolamo, and S. Crewell, 2015: Assessment of small-scale integrated water vapour variability during HOPE. *Atmos. Chem. Phys.*, **15**, 2675–2692, https://doi.org/10.5194/acp-15-2675-2015.

Stelten, S., and W. A. Gallus, 2017: Pristine nocturnal convective initiation: A climatology and preliminary examination of predictability. *Wea. Forecasting*, **32**, 1613–1635, https://doi.org/10.1175/WAF-D-16-0222.1.

Tollerud, E. I., and Coauthors, 2008: Mesoscale moisture transport by the low-level jet during the IHOP field experiment. *Mon. Wea. Rev.*, **136**, 3781–3795, https://doi.org/10.1175/2008MWR2421.1.

Toms, B. A., J. M. Tomaszewski, D. D. Turner, and S. E. Koch, 2017: Analysis of a lower-tropospheric gravity wave train using direct and remote sensing measurement systems. *Mon. Wea. Rev.*, **145**, 2791–2812, https://doi.org/10.1175/MWR-D-16-0216.1.

Trier, S. B., and D. B. Parsons, 1993: Evolution of environmental conditions preceding the development of a nocturnal mesoscale convective complex. *Mon. Wea. Rev.*, **121**, 1078–1098, https://doi.org/10.1175/1520-0493(1993)121<1078:EOECPT>2.0.CO;2.

——, C. A. Davis, D. A. Ahijevych, M. L. Weisman, and G. H. Bryan, 2006: Mechanisms supporting long-lived episodes of propagating nocturnal convection within a 7-day WRF Model simulation. *J. Atmos. Sci.*, **63**, 2437–2461, https://doi.org/10.1175/JAS3768.1.

——, J. W. Wilson, D. A. Ahijevych, and R. A. Sobash, 2017: Mesoscale vertical motions near nocturnal convection initiation in PECAN. *Mon. Wea. Rev.*, **145**, 2919–2941, https://doi.org/10.1175/MWR-D-17-0005.1.

Turner, D. D., and U. Löhnert, 2014: Information content and uncertainties in thermodynamic profiles and liquid cloud properties retrieved from the ground-based Atmospheric Emitted Radiance Interferometer (AERI). *J. Appl. Meteor. Climatol.*, **53**, 752–771, https://doi.org/10.1175/JAMC-D-13-0126.1.

——, and W. G. Blumberg, 2019: Improvements to the AERIoe thermodynamic profile retrieval algorithm. *IEEE J. Sel. Top. Appl. Earth Obs. Remote Sens.*, **12**, 1339–1354, https://doi.org/10.1109/JSTARS.2018.2874968.

——, J. E. M. Goldsmith, and R. A. Ferrare, 2016: Development and applications of the ARM Raman Lidar. *The Atmospheric Radiation Measurement (ARM) Program: The First*

20 Years, Meteor. Monogr., No. 57, https://doi.org/10.1175/AMSMONOGRAPHS-D-15-0026.1.

UCAR/NCAR–EOL, 2015: FP1 ARM Central Facility Radiosonde Data, version 1.0. UCAR/NCAR–Earth Observing Laboratory, accessed 12 November 2018, https://data.eol.ucar.edu/dataset/485.021.

——, 2016a: FP3 NCAR/EOL Water Vapor DIAL, QC data in netCDF, version 2.0. UCAR/NCAR–Earth Observing Laboratory, accessed 29 May 2017, https://doi.org/10.5065/D6SJ1HR1.

——, 2016b: Radar regional 3D mosaic in netCDF format, DBZ and ZDR, version 1.0. UCAR/NCAR–Earth Observing Laboratory, accessed 24 September 2016, https://doi.org/10.5065/D6QR4VHM.

——, 2016c: SkewT Plots from All PECAN Radiosondes, version 1.0. UCAR/NCAR–Earth Observing Laboratory, accessed 16 December 2016, https://data.eol.ucar.edu/dataset/485.123.

Vanderwende, B. J., J. K. Lundquist, M. E. Rhodes, E. S. Takle, and S. L. Irvin, 2015: Observing and simulating the summertime low-level jet in central Iowa. *Mon. Wea. Rev.*, **143**, 2319–2336, https://doi.org/10.1175/MWR-D-14-00325.1.

Wagner, T. J., W. F. Feltz, and S. A. Ackerman, 2008: The temporal evolution of convective indices in storm-producing environments. *Wea. Forecasting*, **23**, 786–794, https://doi.org/10.1175/2008WAF2007046.1.

Walters, C. K., J. A. Winkler, R. P. Shadbolt, J. van Ravensway, and G. D. Bierly, 2008: A long-term climatology of southerly and northerly low-level jets for the Central United States. *Ann. Assoc. Amer. Geogr.*, **98**, 521–552, https://doi.org/10.1080/00045600802046387.

——, ——, S. Husseini, R. Keeling, J. Nikolic, and S. Zhong, 2014: Low-level jets in the North American Regional Reanalysis (NARR): A comparison with rawinsonde observations. *J. Appl. Meteor. Climatol.*, **53**, 2093–2113, https://doi.org/10.1175/JAMC-D-13-0364.1.

Weather Prediction Center, 2015: WPC surface analysis valid for 07/11/2015 at 03 UTC [surface analysis map image]. Weather Prediction Center (WPC), accessed 12 November 2018, https://www.wpc.ncep.noaa.gov/archives/web_pages/sfc/sfc_archive_maps.php?arcdate=07/11/2015&selmap=2015071103.

Weckwerth, T. M., and Coauthors, 2004: An overview of the International H_2O Project (IHOP_2002) and some preliminary highlights. *Bull. Amer. Meteor. Soc.*, **85**, 253–277, https://doi.org/10.1175/BAMS-85-2-253.

——, and U. Romatschke, 2019: Where, when, and why did it rain during PECAN? *Mon. Wea. Rev.*, **147**, 3557–3573, https://doi.org/10.1175/MWR-D-18-0458.1.

——, J. Hanesiak, J. W. Wilson, S. B. Trier, S. K. Degelia, W. A. Gallus, R. D. Roberts, and X. Wang, 2019: Nocturnal convection initiation during PECAN 2015. *Bull. Amer. Meteor. Soc.*, **100**, 2223–2239, https://doi.org/10.1175/BAMS-D-18-0299.1.

Whiteman, C. D., X. Bian, and S. Zhong, 1997: Low-level jet climatology from enhanced rawinsonde observations at a site in the Southern Great Plains. *J. Appl. Meteor.*, **36**, 1363–1376, https://doi.org/10.1175/1520-0450(1997)036<1363:LLJCFE>2.0.CO;2.

Wilson, J. W., and R. D. Roberts, 2006: Summary of convective storm initiation and evolution during IHOP: Observational and modeling perspective. *Mon. Wea. Rev.*, **134**, 23–47, https://doi.org/10.1175/MWR3069.1.

——, S. B. Trier, D. W. Reif, R. D. Roberts, and T. M. Weckwerth, 2018: Nocturnal elevated convection initiation of the PECAN 4 July hailstorm. *Mon. Wea. Rev.*, **146**, 243–262, https://doi.org/10.1175/MWR-D-17-0176.1.

Wulfmeyer, V., H. S. Bauer, M. Grzeschik, A. Behrendt, F. Vandenberghe, E. V. Browell, S. Ismail, and R. A. Ferrare, 2006: Four-dimensional variational assimilation of water vapor differential absorption lidar data: The first case study within IHOP_2002. *Mon. Wea. Rev.*, **134**, 209–230, https://doi.org/10.1175/MWR3070.1.